Active vibration control of a beam subjected to AM or FM disturbances

Peter J. Mucci[a] and Rajendra Singh[b]

(Received 1994 June 06; revised 1995 September 07)

Active control of the vibration of a beam subjected to amplitude- or frequency-modulated disturbances was investigated to determine the feasibility of using this technology to reduce the vibration and noise from geared systems. Two test cases for both amplitude and frequency modulation included on- and off-resonance narrow-band disturbances. A single-input/single-output controller based on an adaptive finite-impulse-response (FIR) filter was used. Analytical studies of actuator and sensor placements and control performance were carried out and an experiment was designed accordingly. A beam structure was fabricated with approximate simply supported boundary conditions to prove the concept. Experimental results were encouraging and showed that complicated vibration spectra could be controlled to some extent. Related issues including comparison between simulation and experiment, and other AM and FM studies are briefly discussed. © ***1995 Institute of Noise Control Engineering.***

Primary subject classification: 38.3; Secondary subject classification: 42

1. INTRODUCTION

Typical vibration spectra of machines contain energy at a number of frequencies. In geared systems, for example, mesh-force modulation phenomena have been observed in measured data. Both amplitude modulation and angle modulation, as well as their combinations, may be observed. The modulation processes produce vibration forces in sidebands about the gear meshing frequency and its harmonics.[1,2] Sound resulting from vibration in the sidebands may have a significant influence on the perceived annoyance of gear whine.[2] The main focus of this paper was an experimental study of the feasibility of actively controlling modulated-vibration disturbances in a resonating structure, specifically a simply supported beam.

Harmonic vibration and sound control has been reported in the literature.[3-6] Some works involving broadband disturbances have also been published.[7,8] Few papers have considered multi-frequency periodic disturbances. Sievers and von Flotow[9] analytically compared different control methods for narrow-band disturbance rejection. Among the limited experimental studies is the work by Chen and Lewis[10] who actively isolated a vibration disturbance consisting of two sinusoids at 40 and 50 Hz using a two-coefficient finite-impulse-response (FIR) filter. Spencer *et al.*[1] studied active vibration control at the gear mesh frequency and its harmonics for a small-scale helicopter transmission.

2. PROBLEM FORMULATION

The scope of this research was strictly limited to application of single-input/single-output (SISO) adaptive feedforward control for minimizing the flexural response of an approximately simply supported beam excited by modulated periodic disturbances. A finite-impulse-response (FIR) digital filter was used to achieve the desired control force by filtering a reference signal correlated with the vibration disturbance. The weights of the filter were adjusted by the filtered-X least-mean-square (LMS) adaptive algorithm[11-13] to minimize the beam's response at an accelerometer error sensor.

Figure 1 shows a block diagram of the control system where the feedforward reference signal f(m) and disturbance signal d(m) were considered to be the same. As a result of the non-unity transfer function C(z) present between the outputs of the FIR filter and error sensor e(m), the reference signal must be pre-filtered by a model $\hat{C}(z)$ of the transfer function before being used in the adaptive algorithm to prevent instability. The result of the pre-filtering was the filtered reference signal $f_f(m)$. The transfer function was modeled by a 25 pole-and-zero infinite-impulse-response (IIR) filter for which the weights were determined off-line before the control began. All control tasks were implemented by means of a Texas Instruments TMS320C30 digital signal processor.

The disturbance signals were amplitude- or frequency-modulated sinusoids where the modulating functions were

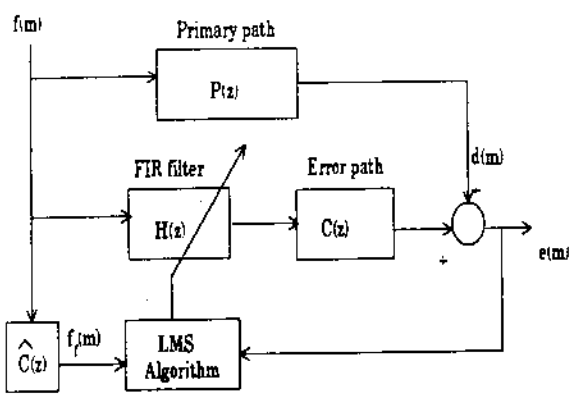

Fig. 1 – Block diagram of feedforward control system.

[a] *Acoustics & Mechanics Technology, The Trane Company, 3600 Pammel Creek Road, La Crosse, Wisconsin 54601, U.S.A.*

[b] *Acoustics & Dynamics Laboratory, Department of Mechanical Engineering, The Ohio State University, 206 West 18th Avenue, Columbus, Ohio 43210-1107, U.S.A.*

Singh_070

also sinusoidal. The amplitude-modulated (AM) signal $F_{AM}(t)$ is given by

$$F_{AM}(t) = A \sin(\omega_c t)[1 + m_0 \sin(\omega_m t)]$$
$$= A\{\sin(\omega_c t) + (m_0/2)\sin[(\omega_c \pm \omega_m)t \pm (\pi/2)]\}, \quad (1)$$

where ω_c and ω_m are the carrier and modulating angular frequencies, respectively, A is the carrier amplitude, and m_0 is the modulation depth, both of which were taken as unity for this study. By means of a trigonometric identity, the signal represented by Eq. (1) can also be expressed as the sum of three signals which shows that the AM signal consists of a carrier and an upper and lower sideband at frequencies $(\omega_c \pm \omega_m)$. The spectrum of the AM signal is shown in Fig. 2(a).

The frequency-modulated (FM) signal $F_{FM}(t)$ is given by

$$F_{FM}(t) = A \cos[\omega_c t + \varphi_m \sin(\omega_m t)]$$
$$= A\left\{ J_0(\varphi_m) \cos(\omega_c t) + \sum_{p=1}^{\infty} (-1)^p J_p(\varphi_m) \times [\cos(\omega_c - p\omega_m)t + (-1)^p \cos(\omega_c + p\omega_m)t] \right\}, \quad (2)$$

where φ_m is the modulation index or maximum phase deviation and $J_p(\varphi_m)$ is the Bessel function of the first kind, of order p, and argument φ_m.[14,15] Equation (2) shows that the FM signal consists of a carrier and an infinite number of sidebands at frequencies $(\omega_c \pm p\omega_m)$. The amplitudes of the carrier and sidebands depend on the appropriate Bessel function. A modulation index of $\varphi_m = 2$, and amplitude A = 1 were used in this study. The spectrum consisting of the carrier and the first five sideband pairs is shown in Fig. 2(b).

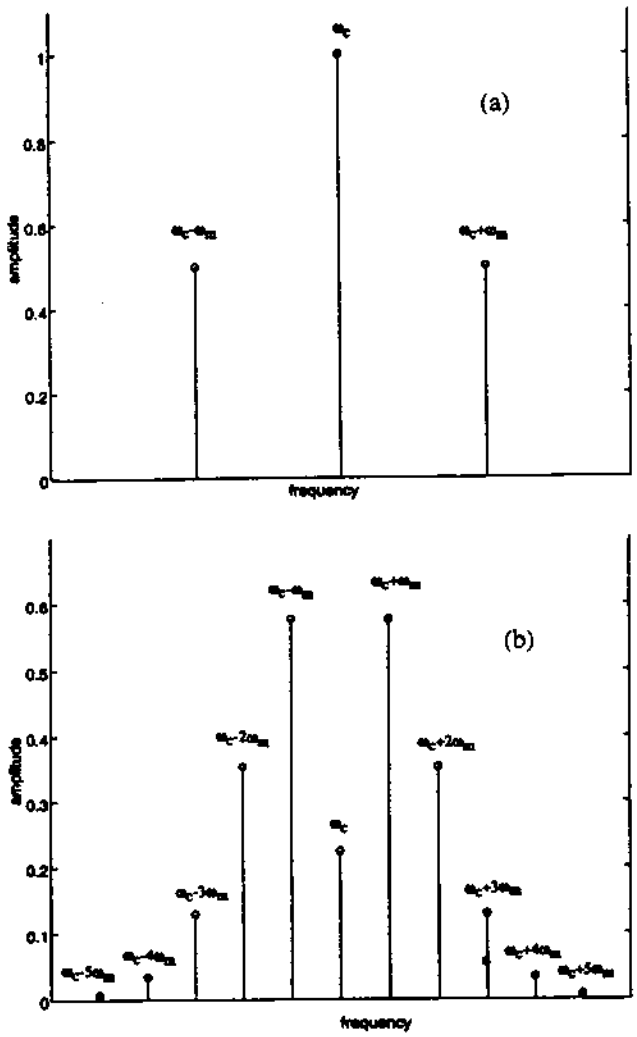

Fig. 2 – Spectra of amplitude-modulated (AM) and frequency modulated (FM) disturbance signals. (a) AM with A=1, m_0=1 in Eq. (1); (b) FM with A=1, φ_m=2 in Eq. (2).

3. ANALYTICAL STUDIES

Before designing an experiment, analytical and computer simulation studies were performed to explore issues pertaining to actuator and sensor placement, and to FIR filter-order selection. The simply supported beam properties and dimensions were chosen so that the first four natural frequencies (ω_n) were 77, 308, 693, and 1231 Hz according to the Euler beam theory.

A. Actuator placement

Figure 3 shows a schematic of the beam setup showing the locations for the disturbance source x_d, control source x_c, and accelerometer error sensor x_a along the beam of length L. The disturbance source was located near the end of the beam (x_d = 0.875 L) where it could excite a large number of modes. The control source and error sensor positions (x_c = 0.75 L, x_a = 0.125 L) were chosen via a semi-analytical study described below such that harmonic disturbances could be attenuated not only at the error sensor, but also over a large portion of the beam at frequencies up to 800 Hz. This control bandwidth included the first three natural frequencies.

Similar to the methodology of Nelson and Elliot,[12] a cost function ϵ was defined by

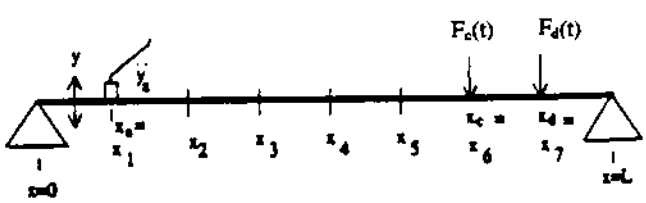

Fig. 3 – Schematic of beam setup showing accelerometer at position 1, disturbance at position 7, and control at position 6.

$$\epsilon = \left(\frac{1}{L}\right)\int_0^L |\ddot{y}(x,t)|^2\,dx = \langle |\ddot{y}(x,t)|^2 \rangle_x. \tag{3}$$

The cost function is a spatial average of the magnitude of the time-varying acceleration $\ddot{y}(x,t)$ over the beam span of length L. Given a primary harmonic disturbance, Eq. (3) will be a quadratic function of the magnitude and phase of the secondary control source relative to the primary source and thus will have a unique minimum.

For a harmonic disturbance $F_d(t)=\bar{F}_d e^{j\omega t}$ at $x = x_d$, where $\bar{F}_d$ is the complex force and ω is the frequency of the disturbance, the steady state displacement response of the beam is given by the modal summation[12,16,17]

$$y_d(x,t)=\sum_{n=1}^{\infty} \frac{1}{m_b(\omega_n^2-\omega^2)+j2\xi_n\omega_n\omega}\frac{\phi_n(x)\phi_n(x_d)}{}\bar{F}_d e^{j\omega t}, \tag{4}$$

where ϕ_n and ω_n are the nth mode shape and natural frequency, respectively, ζ_n is the modal damping ratio, and m_b is the mass of the beam.

Likewise, a control input $F_c(t)=\bar{F}_c e^{j\omega t}$ at $x=x_c$ gives the response

$$y_c(x,t)=\sum_{n=1}^{\infty} \frac{1}{m_b(\omega_n^2-\omega^2)+j2\xi_n\omega_n\omega}\frac{\phi_n(x)\phi_n(x_c)}{}\bar{F}_c e^{j\omega t}. \tag{5}$$

Superposition of the disturbance and control-input displacement responses gives

$$\begin{aligned} y(x,t) &= y_d(x,t)+y_c(x,t) \\ &= \sum_{n=1}^{\infty} \frac{1}{m_b(\omega_n^2-\omega^2)+j2\xi_n\omega_n\omega}\frac{\phi_n(x)e^{j\omega t}}{} \\ &\quad \times[\bar{F}_d\phi_n(x_d)+\bar{F}_c\phi_n(x_c)] \\ &= \sum_{n=1}^{\infty} a_n\phi_n(x)e^{j\omega t}, \end{aligned} \tag{6}$$

where the coefficients are given by

$$a_n=\frac{1}{m_b(\omega_n^2-\omega^2)+j2\xi_n\omega_n\omega}\frac{\bar{F}_d\phi_n(x_d)+\bar{F}_c\phi_n(x_c)}{} = a_{dn}+a_{cn}\bar{F}_c. \tag{7}$$

For a harmonic disturbance, the cost function in Eq. (3) can be expressed as

$$\epsilon(\omega)=\frac{\omega^4}{L}\int_0^L y^*(x,t)y(x,t)\,dx. \tag{8}$$

Substituting Eq. (6) into Eq. (8) yields

$$\begin{aligned} \epsilon(\omega) &= \frac{\omega^4}{L}\int_0^L\left[\sum_{n=1}^{\infty} a_n\phi_n(x)\right]^*\left[\sum_{m=1}^{\infty} a_m\phi_m(x)\right]dx \\ &= \omega^4\sum_{n=1}^{\infty}|a_n|^2, \end{aligned} \tag{9}$$

where the superscript asterisk indicates the complex conjugate and use was made of the modal orthogonality property defined by

$$\frac{1}{L}\int_0^L \phi_m(x)\phi_n(x)\,dx=\delta_{mn}, \tag{10}$$

where δ_{mn} is the Kronecker delta, i.e., $\delta_{mn}=1$ when $m=n$, otherwise it is equal to zero.

With Eq. (7), the cost function of Eq. (9) can be expressed as a quadratic function of $\bar{F}_c$ according to

$$\begin{aligned} \epsilon(\omega) &= \omega^4\sum_{n=1}^{\infty}|a_{dn}+a_{cn}\bar{F}_c|^2 \\ &= \omega^4\sum_{n=1}^{\infty}(a_{dn}+a_{cn}\bar{F}_c)(a_{dn}+a_{cn}\bar{F}_c)^* \\ &= \omega^4\left[\bar{F}_c^*\left(\sum_{n=1}^{\infty}|a_{cn}|^2\right)\bar{F}_c+\bar{F}_c^*\left(\sum_{n=1}^{\infty}a_{cn}^*a_{dn}\right)\right. \\ &\quad \left.+\left(\sum_{n=1}^{\infty}a_{cn}^*a_{dn}\right)^*\bar{F}_c+\sum_{n=1}^{\infty}|a_{dn}|^2\right]. \end{aligned} \tag{11}$$

The control force $\bar{F}_c$ that minimizes the cost function in Eq. (11) is given by

$$\bar{F}_{c(opt)}=\frac{-\sum_{n=1}^{\infty}a_{cn}^*a_{dn}}{\sum_{n=1}^{\infty}|a_{cn}|^2} \tag{12}$$

to yield the minimum cost function ϵ_{min} given by

$$\epsilon_{min}=\omega^4\left[\sum_{n=1}^{\infty}|a_{dn}|^2-\left(\frac{|\sum_{n=1}^{\infty}a_{cn}^*a_{dn}|^2}{\sum_{n=1}^{\infty}|a_{cn}|^2}\right)\right]. \tag{13}$$

The expression in Eq. (13) was evaluated at different frequencies for a given actuator location to determine the maximum attenuation over the beam span for various actuator locations until a suitable actuator position was found. The most-effective control can be achieved by collocating the control and disturbance sources. In this case, the optimal control source would have the same magnitude as the disturbance and 180-deg phase difference, i.e., $\bar{F}_c=-\bar{F}_d$, and the minimum of the cost function in Eq. (13) would be zero for all frequencies.

Figure 4 shows the calculated value of the cost function evaluated without control and the minimum of the cost function for different frequencies. The control actuator was located at $x=0.125$ L, so that the disturbance and control were symmetric about the center of the beam. A modal damping ratio $\zeta_n=0.01$ was used for all modes. Only resonances were controlled for this actuator position, while the anti-resonances were almost unaffected. This result occurred because, at the resonances, the beam response was dominated by one mode and the control action reduced this contribution until the residual modes became significant.[12] In between resonances, there were a large number of modes contributing to the response, and since the modal excitation caused by the disturbance and control sources was in phase for the odd modes and out of phase for the even modes, little control was possible because the control action that decreased the amplitude of the odd modes increased the amplitude of the even modes, and vice-versa.

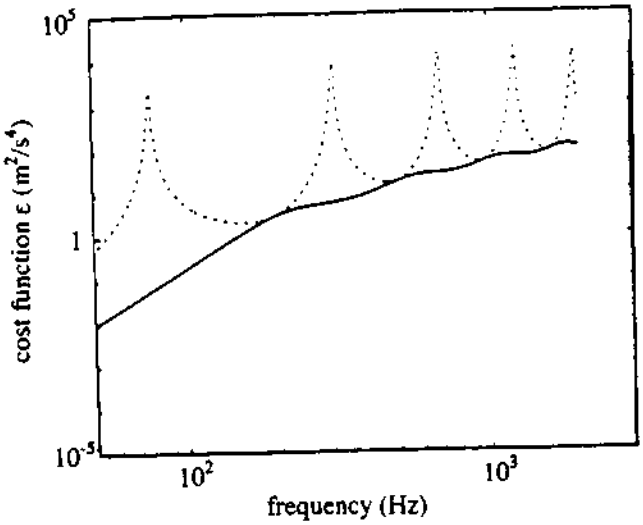

Fig. 4 – Cost function ϵ of Eq. (3) with control actuator at $x = x_c$=0.125 L. ····· no control; — minimizing the cost function.

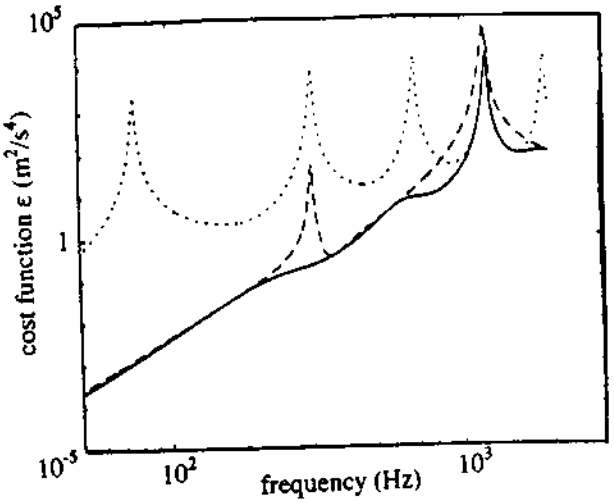

Fig. 5 – Cost function with control actuator at $x = x_c$=0.75 L, accelerometer at $x = x_a$=0.5 L. ····· no control; — minimizing the cost function; ---- minimizing mean-square acceleration at the sensor location.

In Fig. 5 (solid line) the actuator was located at x=0.75 L. Attenuation at all frequencies was possible up to approximately 800 Hz and included the first three resonances with decreasing control ability as the fourth natural frequency was approached. Since the actuator was located on a node of the fourth mode, control in the frequency range around this mode was not possible. Control was, however, possible at the anti-resonances as well as the resonances at frequencies less than 800 Hz because the control source was relatively close to the disturbance and could couple into the first three modes with the same phase as the disturbance. At frequencies above the fourth natural frequency, the actuator only would be able to control resonances, provided that the actuator was not on a node of the mode shape for that resonance. In general, the closer the control source is to the disturbance, the larger the frequency bandwidth of the disturbances it will be able to control. When the control and disturbance are collocated, the theoretical bandwidth will be infinite.

B. Sensor placement

The above analysis provided a method for evaluating actuator placement to minimize the global acceleration ϵ of the beam. To implement a controller that minimized ϵ would require measurement of acceleration over the whole extent of the beam, which was impractical. To overcome this problem, a discrete sensor was used to measure the acceleration at a point, and if properly placed, the result of minimizing the output of the sensor should be close to the optimal minimization.

The response given in Eq. (6) can be set equal to zero at $x=x_a$ by specifying the cohtrol force as

$$\bar{F}_c = -\left[\frac{\sum_{n=1}^{\infty} A_n \phi_n(x_a)\phi_n(x_d)}{\sum_{n=1}^{\infty} A_n \phi_n(x_a)\phi_n(x_c)}\right]\bar{F}_d, \qquad (14)$$

where the amplitude function coefficients are found from

$$A_n = \frac{1}{m_b}\frac{1}{(\omega_n^2-\omega^2)+j2\xi_n\omega_n\omega}. \qquad (15)$$

Note that for a harmonic disturbance, minimizing displacement, velocity, or acceleration will yield identical results. After finding the control force $\bar{F}_c$ from Eq. (14), the force can be substituted into the cost function of Eq. (11) to determine if this local minimization will produce global attenuation.

The dashed line in Fig. 5 shows the cost function ϵ when the acceleration $\psi_a^2=|\ddot{y}_a|^2$ was minimized at the middle of the beam (at x_a=0.5 L) for the actuator at x_c=0.75 L. This

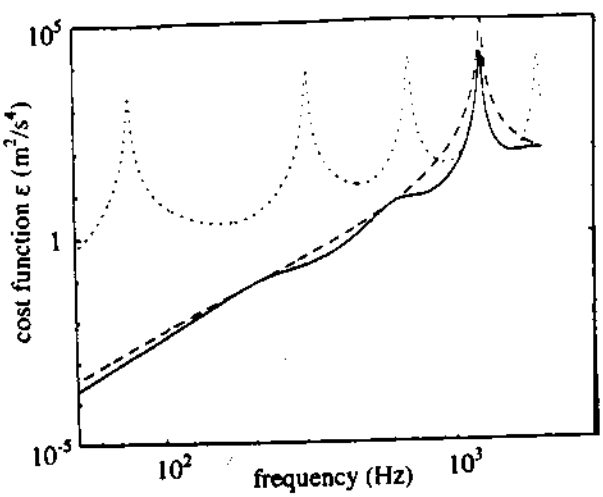

Fig. 6 – Cost function with control actuator at $x = x_c$=0.75 L, accelerometer at $x = x_a$=0.125 L. ····· no control; — minimizing the cost function; ---- minimizing mean-square acceleration at the sensor location.

position was a poor choice for the sensor location because it could not observe the even modes. The result was the spike at the second mode and the amplification at the fourth mode that did not occur when the cost function was minimized directly.

For the same actuator position at x_c=0.75 L, the sensor was then placed at x_a=0.125 L. Figure 6 shows that minimizing the sensor acceleration response ψ_a^2 at x_a=0.125 L produced a result similar to minimizing the cost function in this case because the sensor was located near the end of the beam where it could observe many modes. The actuator and sensor configuration for Fig. 6 were used in the computer simulations and experiments as vibration control seemed possible at all frequencies up to approximately 800 Hz.

It could be argued that the actuator configuration used for the results in Fig. 4 (with the actuator at x_c=0.125 L) was superior to that used for Fig. 6 (with the actuator at x_c=0.75 L) because that location permitted control of all resonances and controlling resonances is more important than controlling off-resonance disturbance. Because the focus of this work was the control of modulated disturbances with sidebands up to 800 Hz, which entailed controlling resonance and nonresonance frequencies simultaneously, the actuator position used for Fig. 6 was more appropriate. More importantly, Fig. 7 shows the effect on cost function ϵ when the output of a sensor located at x_a=0.125 L was minimized for the actuator position x_c=0.125 L. Figure 7 shows that the control action required to drive the sensor response to zero caused the resonances to move to positions between the original resonances, with strong resonances remaining at some frequencies. This configuration would be virtually useless for controlling modulated disturbances and additional sensors would be necessary for good control of beam vibration.

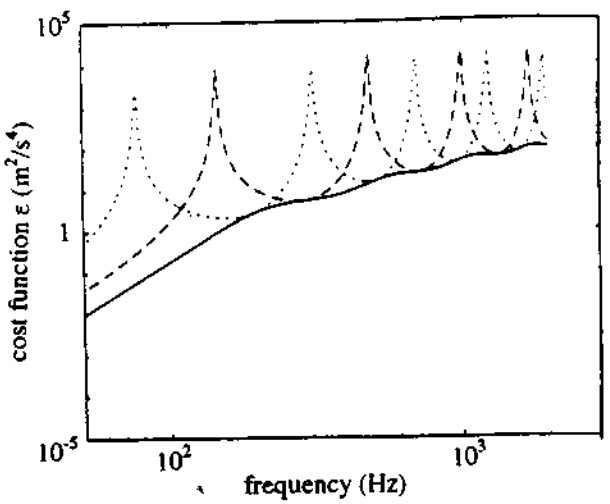

Fig. 7 – Cost function with control actuator at $x = x_c$=0.125 L, accelerometer at $x = x_a$=0.125 L. ····· no control; — minimizing the cost function; ---- minimizing mean-square acceleration at the sensor location.

4. COMPUTER SIMULATIONS

Numerical simulations were performed to aid in the selection of the order of the FIR filters. The simply supported beam of Fig. 3 was modeled as follows. Because the undamped natural frequencies ω_n and modes ϕ_m were known from the analytical solutions, a modal identification analysis was performed to determine the mass **M** and stiffness **K** matrices for a lumped-mass model of the beam by evaluating the analytical modes shapes at N_m discrete points on the beam, forming the discrete normal modal matrix $\mathbf{\Phi}$ of dimension N_m.

The following transformations[16] were used for the proportionately damped system of modal damping ratios ξ_n:

$$\mathbf{\Phi}^T\mathbf{M}\mathbf{\Phi} = I, \tag{16}$$

$$\mathbf{\Phi}^T\mathbf{K}\mathbf{\Phi} = \Omega = \text{diag}[\omega_n^2], \quad \text{for } n = 1,2,\ldots,N_m, \tag{17}$$

$$\mathbf{\Phi}^T\mathbf{C}\mathbf{\Phi} = \text{diag}[2\xi_n\omega_n], \quad \text{for } n = 1,2,\ldots,N_m, \tag{18}$$

where Ω is the eigenvalue matrix, **M**, **K**, and **C** are the mass, stiffness, and damping matrices respectively, that must be determined, **I** is the N_m by N_m identity matrix, N_m is the number of modes, and superscript T indicates matrix transposition.

A modal damping ratio ζ_i=0.01 was assumed for all modes so that the **M**, **K**, and **C** matrices were found as follows:

$$\mathbf{M} = \Lambda\mathbf{\Phi}^{-T}\mathbf{\Phi}^{-1} = \text{diag}\{[m_b/(N_m+1)]_i\}, \quad \text{for } i = 1,2,\ldots,N_m \tag{19}$$

$$\mathbf{K} = \Lambda\mathbf{\Phi}^{-T}\Omega\mathbf{\Phi}^{-1}, \tag{20}$$

$$\mathbf{C} = \Lambda\mathbf{\Phi}^{-T}\,\text{diag}[2\xi_i\omega_i]\mathbf{\Phi}^{-1}. \tag{21}$$

The scaling factor Λ was included because the mode shapes and natural frequencies contained only relative information as far as the stiffness and mass matrices were concerned. The scaling factor was defined as

$$\Lambda = \{[N_m/(N_m+1)]m_b\}/\text{tr}[\mathbf{\Phi}^{-T}\mathbf{\Phi}^{-1}] \tag{22}$$

so that the fraction $1/(N_m + 1)$ of the physical mass of the beam was added to the supports and was assumed stationary. The result is a diagonal mass matrix with nondiagonal stiffness and damping matrices. The operator tr performs the trace of the product of the matrices.

The equations of motion were expressed as N_m coupled ordinary differential equations given by

$$\mathbf{M}\ddot{\mathbf{y}}(t) + \mathbf{C}\dot{\mathbf{y}}(t) + \mathbf{K}\mathbf{y}(t) = \mathbf{F}(t), \tag{23}$$

where $\mathbf{y}(t)$ is a $(N_m \times 1)$ column vector of displacements and $\mathbf{F}(t)$ is a $(N_m \times 1)$ column vector of forces.

To facilitate the computer simulations, Eq. (23) must be expressed in the state space of dimension $2N_m$. To accomplish this task, a $2N_m \times 1$ state vector $\mathbf{z}$ was defined where

$$z_i = \begin{cases} \mathbf{y}_{(i+1)/2}, & \text{for } i \text{ odd} \\ \dot{\mathbf{y}}_{i/2}, & \text{for } i \text{ even} \end{cases} \tag{24}$$

With Eq. (24), the state equations become

$$\dot{\mathbf{z}}(t) = \mathbf{A}\mathbf{z}(t) + \tilde{\mathbf{F}}(t), \tag{25}$$

where the matrix of coefficients is given by

$$\mathbf{A}=\begin{bmatrix} 0 & 1 & 0 & 0 & \cdots & 0 & 0 \\ \frac{-k_{11}}{m_{11}} & \frac{-c_{11}}{m_{11}} & \frac{-k_{12}}{m_{11}} & \frac{-c_{12}}{m_{11}} & \cdots & \frac{-k_{1n}}{m_{11}} & \frac{-c_{1n}}{m_{11}} \\ 0 & 0 & 0 & 1 & 0 & \cdots & 0 \\ \frac{-k_{21}}{m_{22}} & \frac{-c_{21}}{m_{22}} & \frac{-k_{22}}{m_{22}} & \frac{-c_{22}}{m_{22}} & \cdots & \frac{-k_{2n}}{m_{22}} & \frac{-c_{2n}}{m_{22}} \\ \vdots & \vdots & \vdots & \vdots & \cdots & \vdots & \vdots \\ 0 & 0 & 0 & 0 & \cdots & 0 & 1 \\ \frac{-k_{n1}}{m_{nn}} & \frac{-c_{n1}}{m_{nn}} & \frac{-k_{n2}}{m_{nn}} & \frac{-c_{n2}}{m_{nn}} & \cdots & \frac{-k_{nn}}{m_{nn}} & \frac{-c_{nn}}{m_{nn}} \end{bmatrix} \tag{26}$$

and the matrix of forces is given by

$$\tilde{\mathbf{F}}=\begin{bmatrix} 0 \\ \frac{f_1(t)}{m_{11}} \\ 0 \\ \frac{f_2(t)}{m_{22}} \\ \vdots \\ 0 \\ \frac{f_{N_m}(t)}{m_{N_mN_m}} \end{bmatrix}. \tag{27}$$

With the beam described in state-variable form, computer simulations were performed to estimate the size of the FIR filters that were necessary for different modulated disturbances. Although studies of FIR filter-order selection could have been carried out with the modal expansion description of the beam given earlier, it was also desired to test the transient performance of the least-mean-squares algorithm which required a simulation.

Referring to Fig. 1, it can be shown[12,13] that the optimal FIR filter coefficients are given by

$$\mathbf{h}_{\text{opt}}=\begin{bmatrix} h_{0(\text{opt})} \\ h_{1(\text{opt})} \\ \vdots \\ h_{N-1(\text{opt})} \end{bmatrix}=\mathbf{R}^{-1}\mathbf{r}=\mathbf{R}^{-1}\begin{bmatrix} R_{f_fd}(0) \\ R_{f_fd}(1) \\ \vdots \\ R_{f_fd}(N-1) \end{bmatrix}, \tag{28}$$

where $\mathbf{h}_{\text{opt}}$ is the vector of optimal FIR coefficients, N is the number of filter coefficients, and the matrix $\mathbf{R}$ was defined as

$$R=\begin{bmatrix} R_{f_ff_f}(0) & R_{f_ff_f}(1) & \cdots & R_{f_ff_f}(N-1) \\ R_{f_ff_f}(1) & R_{f_ff_f}(0) & \cdots & R_{f_ff_f}(N-2) \\ \vdots & \vdots & \cdots & \vdots \\ R_{f_ff_f}(N-1) & R_{f_ff_f}(N-2) & \cdots & R_{f_ff_f}(0) \end{bmatrix} \tag{29}$$

where $R_{f_ff_f}(k)$ is the autocorrelation of the filtered reference signal f_f at a time lag of k samples, and $R_{f_fd}(k)$ is the cross correlation between f_f and the primary vibration d at a time lag of k samples.

Examining Eq. (28), it is seen that if the $\mathbf{R}$ matrix is singular, the problem is over-determined and there are more filter coefficients than are necessary. Singularity of the $\mathbf{R}$ matrix also indicates that convergence difficulties will occur when the problem is solved using the least-mean-squares algorithm due to the zero eigenvalues of the $\mathbf{R}$ matrix because convergence time is proportional to the ratio of the largest to the smallest eigenvalue.[13]

The rank of the $\mathbf{R}$ matrix is determined by the spectral characteristics of the reference signal $\mathbf{f}(m)$. Theoretically, the $\mathbf{R}$ matrix has rank $2N_f$, where N_f is the number of frequency components in the reference signal.[18] In practice, near singularity of the $\mathbf{R}$ matrix is also problematic and can occur even though there are more than $0.5N$ frequency components in a reference signal. In some cases, experimenting with filter size empirically may be the only reliable method to determine the rank of the $\mathbf{R}$ matrix.

In general, filters of too small order cannot sufficiently attenuate multiple frequency components simultaneously, while filters of too large order experience slowed convergence and reduced active-control performance. Also, as time-varying terms of the adaptive process could not be eliminated by synchronous sampling of the reference signal at the appropriate sampling frequency because of the nature of a modulated signal, more coefficients may be necessary in the filter to minimize the time varying terms. Clark and Gibbs present a good analysis of this concept in Ref. 19.

Computer simulations were performed with the beam considered as seven equally spaced lumped masses and the above inversion procedure was used to find the optimal FIR filter for a given modulated disturbance and filter size. Increasing the filter size produced better attenuation of the error signal until a point where further increases yielded reduced attenuation as a consequence of numerical problems in the inversion of the $\mathbf{R}$ matrix. The filter size that produced the greatest attenuation was taken to be the best filter for the particular disturbance.

Computer simulations were then performed using the LMS algorithm to find the optimal FIR filter coefficients in order to test the algorithm's ability to attenuate modulated disturbances and to test the above filter-order selection process. Overall, the simulations produced good results. In some cases, the attenuations achieved appeared as though they could be improved. In those cases, larger and smaller filters than those determined above were used with the only result being degraded performance. Thus, the filter selection process seemed to be reliable and predicted that filters of order six and less were best for the disturbances considered in the study.

5. BEAM FABRICATION AND MODAL TESTS

The beam's physical properties and dimensions are shown in Table 1. The ends of the beam were attached to a supporting structure using thin shims that resisted translation but were relatively compliant to rotation, thus approximating the simply supported boundary conditions reasonably well.[20] Measured natural frequencies ω_n and modal damping ratios ζ_n of the beam are given in Table 1 along

TABLE 1 – Natural frequencies, modal damping ratios, and physical properties for the experimental test beam.

	Without shakers			With two shakers	
	Theory	Experiment		Experiment	
Modal index (n)	f_n(Hz)	f_n(Hz)	ζ_n(%)	f_n(Hz)	ζ_n(%)
1	77	76	0.66	76	6.00
2	308	302	0.17	266	3.11
3	693	668	0.22	618 ± 15	2.14
4	1231	1180	1.33	812 ± 10	3.39
5	...	...	...	1180 ± 20	1.42
Material:		Carbon steel		Length (L): 381 mm	
Density (ρ):		7850 kg/m^3		Width: 38.1 mm	
Young's modulus (E):		210 Gpa		Thickness: 4.7625 mm	

with predicted values of ω_n. In addition to the measured natural frequencies being within 4% of the theoretical frequencies, the measured mode shapes also agreed well with the theoretical.

Disturbance $F_d(t)$ and control $F_c(t)$ forces were applied to the beam by means of electrodynamic shakers that were hung from the supporting structure with elastic cords and attached to the beam with 229-mm-diam nylon stingers as shown in Fig. 8. Once the shakers were attached to the beam, the natural frequencies were changed and the damping ratios were increased as shown in Table 1 as a result of the change in the beam's boundary conditions. Variations in the third through fifth natural frequencies were observed when the shakers were detached and then reattached to the beam. Estimates of the variability are also shown in Table 1.

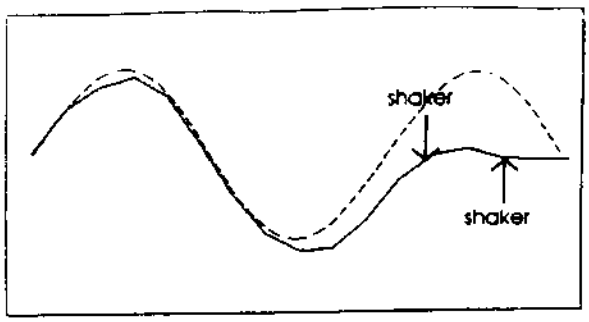

Fig. 9 – Shape of the third vibration mode. ---- simply supported beam (theory); — experiment with shakers attached.

In addition to changes in the natural frequencies caused by the shaker dynamics, some of the mode shapes were affected as well. The first two mode shapes were relatively unaffected while the third simply supported mode was split into two modes. The first of the split modes (mode 3) is shown in Fig. 9 which shows reduced displacement in the vicinity of the shakers. The second split mode (mode 4) was similar to mode 3 of a simply supported beam with slightly increased displacement in the vicinity of the shakers. The decreased and increased displacements in the vicinity of the shakers for modes 3 and 4, respectively, were thought to be caused by the shakers moving out of phase and in phase, respectively. With the shakers attached, the mode shapes were complex valued, probably because of localized damping provided by the shakers as evidenced by

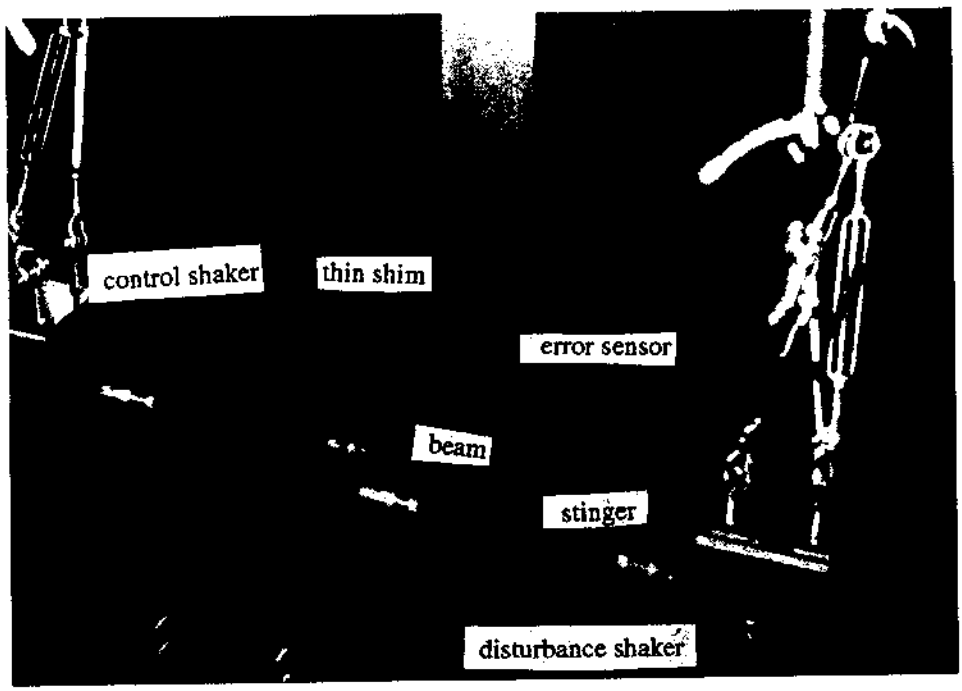

Fig. 8 – Experimental setup for the test beam showing attachment of electrodynamic shakers by stingers and the location of the accelerometer for the error-signal sensor.

the increased damping ratios. The complex valued modes and the reduced displacement of the third mode shape near the control shaker may cause control problems, such as reduced bandwidth, especially when the third mode is significantly excited.

6. EXPERIMENTAL PROCEDURE

Two AM and two FM cases, one on-resonance and one off-resonance as listed in Table 2, were studied. For all cases, the modulating waveform was a 15-Hz sinusoid that created a relatively narrow-band excitation. For the on-resonance cases, the carrier was at 266 Hz which was the second natural frequency of the beam with the shakers attached. (The second natural frequency of 308 Hz for the computer simulations in Sec. 3 was for the beam without shakers attached.) In the off-resonance AM case, the disturbance spectrum was between the second and third resonances. In the off-resonance FM case, the most-significant part of the disturbance spectrum was between the second and third resonances.

Reference and disturbance waveforms were generated on the digital signal processor chip. The reference signal was never converted to an analog signal but was used directly in the computer control code so as to eliminate any corruption by background noise. The disturbance signal (which was the same as the reference signal) was converted to an analog signal and amplified before reaching the disturbance shaker.

For each case, an accelerometer measured the vibration at seven evenly spaced interior points on the beam not including the beam ends. As shown in Fig. 3, accelerations were measured at positions $i=1-7$ with x_i coordinates of 0.125 L, 0.25 L, 0.375 L, 0.5 L, 0.625 L, 0.75 L, and 0.875 L. The mean-square acceleration and the acceleration power spectrum without control were recorded at each point.

Before control could be applied, the FIR filter size needed to be determined. In some cases, the LMS algorithm converged in a matter of seconds while in other cases a large attenuation of the error signal initially occurred followed by a slow, gradual attenuation that could eventually have become significant. In view of this observation, a time limit for convergence of the LMS algorithm was set arbitrarily at 90 s after which time the convergence coefficient was set to zero.

To determine the filter size for each case, a two-coefficient filter initially was tried with the convergence coefficient set so that a fast, yet stable convergence was achieved and the mean-square attenuation of the error signal was then measured. The order of the filter was then raised in increments of two with the convergence coefficient decreased by a factor of $0.5\,N$ to ensure stability, where N is the number of filter coefficients. The mean-square attenuation was then measured. The filter order was increased until the filter that produced the most attenuation in the 90-s time limit was found. After the best filter was found according to the above criteria, the computation was allowed to converge for 90-s and then the accelerations were measured at the seven locations.

A global (spatially averaged) mean-square acceleration attenuation ΔL_a in decibels was defined by

$$\Delta L_a = 10\ \lg\left(\frac{\sum_{i=1}^{7}\langle \ddot{y}_{nc}^2(x_i,t)\rangle_t}{\sum_{i=1}^{7}\langle \ddot{y}_{ac}^2(x_i,t)\rangle_t}\right), \tag{30}$$

where subscripts nc and ac stand for "no control" and "after control," respectively.

TABLE 2 – Modulated disturbance cases studied; Case 1: on-resonance; Case 2: off-resonance.

	Carrier and modulation frequencies	
Modulation type	Case 1	Case 2
AM	f_c=266 Hz= f_2	f_c=355 Hz
	f_m=15 Hz	f_m=15 Hz
FM	f_c=266 Hz=f_2	f_c=355 Hz
	f_m=15 Hz	f_m=15 Hz

7. EXPERIMENTAL RESULTS

A. AM Case 1

For the AM Case 1, a 266-Hz (second natural frequency) carrier sinusoid ω_c was amplitude modulated by a 15-Hz sinusoid ω_m producing lower and upper sidebands about the carrier at 251 and 281 Hz, respectively. Figure 10(a) shows the power spectrum of disturbance reference signal f(m) and Fig. 10(b) shows the power spectrum of the error signal e(m) before control. In addition to the part of the error-signal spectrum that was correlated with the f(m) signal, there were also unintended sidebands and harmonics present. The unintended sidebands, which were the result of unintentional modulation processes, and the harmonics,

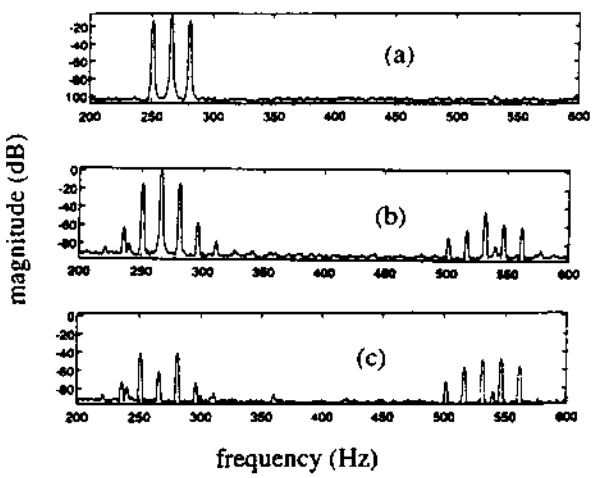

Fig. 10 – Magnitude of the auto-power spectra of acceleration for AM Case 1. Power spectrum magnitude is in decibels relative to an arbitrary reference acceleration. (a) disturbance and reference signal; (b) error signal before control; and (c) error signal after control.

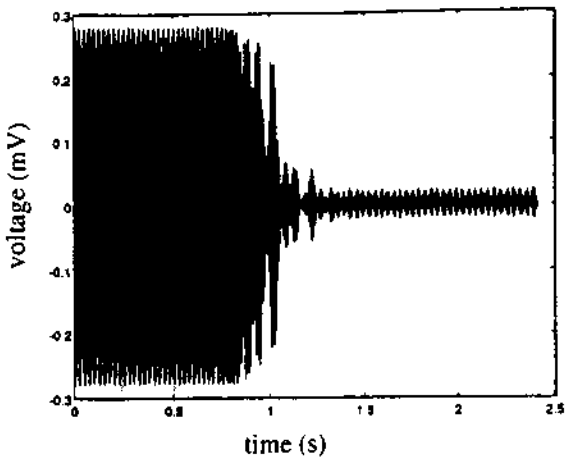

Fig. 11 – Convergence of error signal with time after start for AM Case 1.

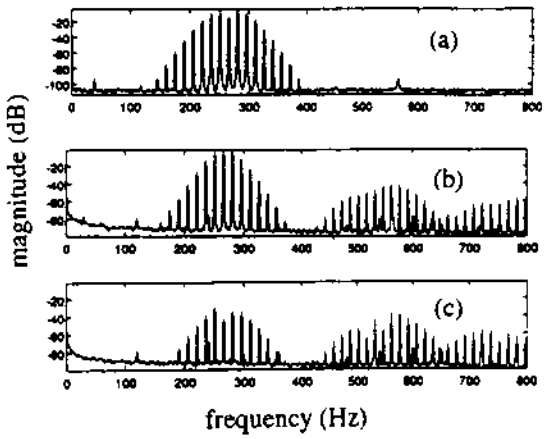

Fig. 13 – Magnitude of the auto-power spectra of acceleration for FM Case 1. (a) disturbance and reference signal; (b) error signal before control; and (c) error signal after control.

which were caused by non-linearities in the experimental setup, were uncorrelated with the f(m) signal and should, on average, not be affected by control. It is possible however that some of the uncorrelated part of the e(m) spectrum was attenuated and that some was amplified after control. It should be noted that what is shown in the plots and termed the disturbance-reference signal is actually the disturbance signal. The reference signal was identical to the disturbance signal except that it had a lower noise floor because it was never converted to an analog signal.

A 6th-order FIR filter was found to give the best attenuation in 90 s for this disturbance, which was not surprising due to the three frequency components of f(m). The e(m) power spectrum after control is shown in Fig. 10(c). The correlated part of e(m) was well attenuated after control was applied. The harmonics were slightly amplified, while the unintended sidebands were attenuated slightly. The time variation of the convergence of e(m) is shown in Fig. 11. In this case, a quick convergence was achieved in approximately 1.3 s.

Figure 12 shows that the mean-square acceleration level, in decibels relative to an arbitrary reference acceleration, was reduced by at least 20 dB at all measurement locations on the beam with the greatest attenuation in the vicinity of the error sensor at position 1. The shape of the mean-square acceleration level before control showed the large contribution from the second mode as evidenced by its similarity to the square of the second mode shape. The spatially averaged mean-square acceleration attenuation for this AM Case 1 was 30 dB. Although not shown, each of the three frequency components of e(m) that were correlated with f(m) were attenuated by 20 dB as well at all measurement locations on the beam.

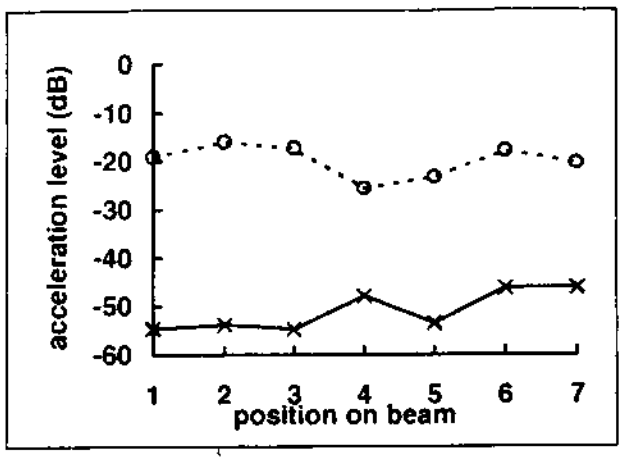

Fig. 12 – Mean-square acceleration level across the span of the beam for AM Case 1. Acceleration level is in decibels relative to an arbitrary reference acceleration. ⊙ no control; × after control.

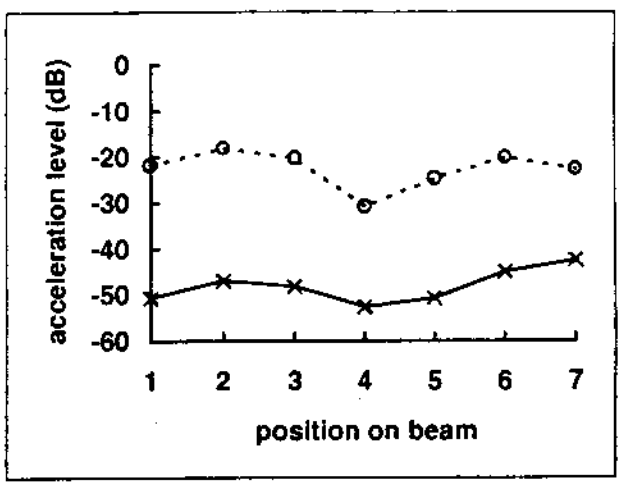

Fig. 14 – Mean-square acceleration level across the span of the beam for FM Case 1. ⊙ no control; × after control.

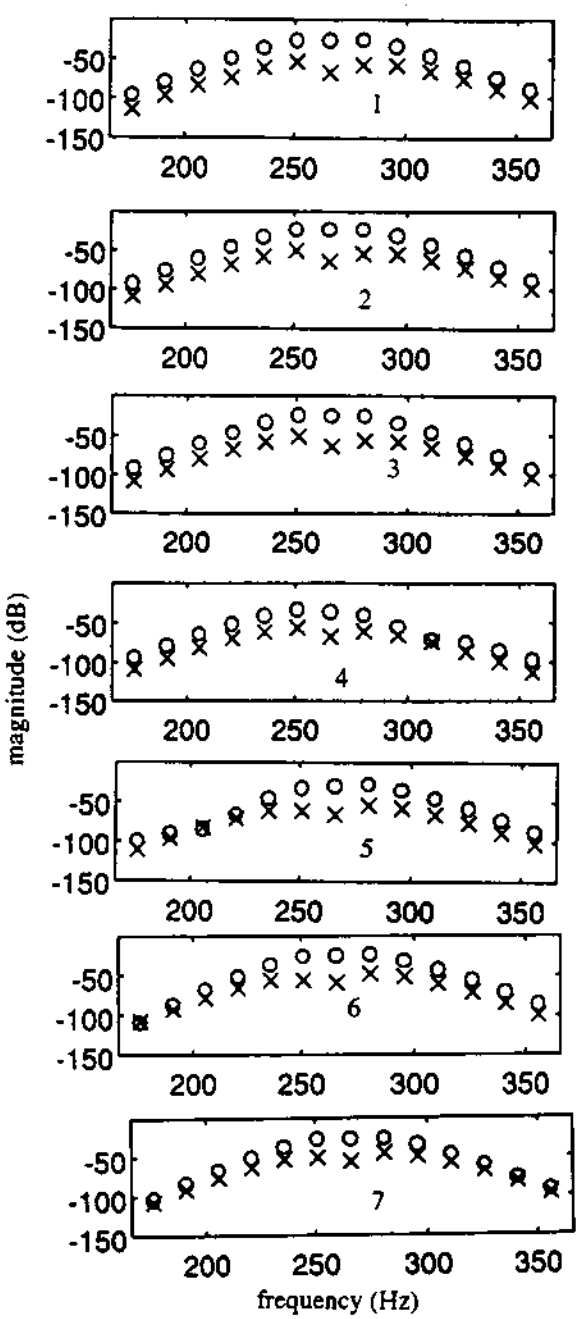

Fig. 15 – Magnitude of the auto-power spectra of acceleration at each beam position for FM Case 1. ⊙ no control; × after control.

B. FM Case 1

For the FM Case 1, the frequencies ω_c and ω_m were the same as in AM Case 1 (266 and 15 Hz, respectively), but frequency modulation was employed. Frequency modulation caused the carrier frequency to be surrounded by a number of lower and upper sidebands as seen in Fig. 13(a) which shows the f(m) power spectrum. Figure 13(b) shows the e(m) power spectrum before control, and again many uncorrelated harmonics were present. Figure 13(c) shows that the correlated part of the e(m) spectrum was well attenuated after control was applied. Some uncorrelated harmonics were amplified while others were attenuated. Control was performed in this case with a six-coefficient filter that was found to give the best performance in the 90-s convergence time limit. Figure 13(c) shows that a large number (at least 13) of the frequency components were attenuated in the error signal spectrum using only the 6th-order filter.

Figure 14 shows the mean-square acceleration level before and after control across the span of the beam. The mean-square acceleration level before control again was similar to the square of the second mode shape because of the large contribution from the second mode. The acceleration level at all measurement locations was attenuated by at least 20 dB with the best attenuation near the error sensor at position 1. The global mean-square acceleration attenuation for this case was 25 dB.

Figure 15 shows the acceleration power spectrum evaluated at each individual frequency component that was correlated with f(m) for all seven positions on the beam. This figure shows that the carrier and first six sideband pairs were attenuated at almost all measurement locations on the beam. The only exceptions were at x_5 where the fourth lower sideband was slightly amplified and x_6 where the sixth lower sideband was amplified slightly. These amplifications had a negligible impact because the amplitudes of the sidebands were already small before control.

C. AM Case 2

For the AM case 2, the carrier frequency was 355 Hz and the frequency of the amplitude modulation was 15 Hz creating a narrowband, off-resonance excitation. Figures 16(a) and (b) show the power spectra of f(m) and e(m) before control, respectively. Figure 16(c) shows that the correlated part of the e(m) spectrum was well attenuated after control was applied. In this case, an eight-coefficient filter gave the best results.

Figure 17 shows the mean-square acceleration level before and after control for the AM Case 2. The mean-square acceleration level before control seemed to still have a sig-

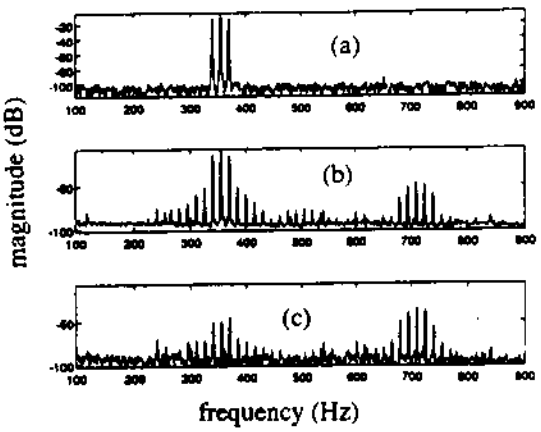

Fig. 16 – Magnitude of the auto-power spectra of acceleration for AM Case 2. (a) disturbance and reference signal; (b) error signal before control; and (c) error signal after control.

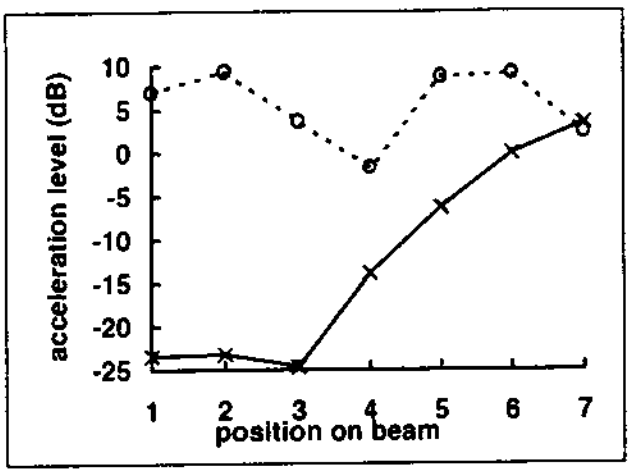

Fig. 17 – Mean-square acceleration level across the span of the beam for AM Case 2. ⊙ no control; × after control.

nificant contribution from the second mode as evidenced by the reduced acceleration at the center of the beam and overall similarity to the square of the second mode shape even though the excitation was well away from the second resonance. The greatest attenuation occurred in the vicinity of the error sensor with about 30-dB attenuation between x_1 and x_3 and steadily decreasing attenuation between x_3 and x_7, with the acceleration slightly amplified at x_7.

The global acceleration-level attenuation was 10 dB, which is much less than in the previous two cases. The smaller attenuation was the result of the off-resonance condition that, according to Fig. 6, was predicted to permit only moderate global acceleration-level attenuation compared with an on-resonance excitation. The attenuation of the individual frequency components at each measurement location on the beam was similar to the mean-square acceleration-level attenuation.

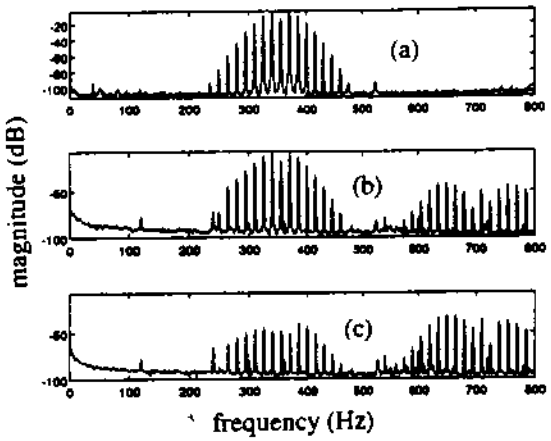

Fig. 18 – Magnitude of the auto-power spectra of acceleration for FM Case 2. (a) disturbance and reference signal; (b) error signal before control; and (c) error signal after control.

D. FM Case 2

For the FM Case 2, a carrier sinusoid at 355 Hz was frequency modulated by a 15-Hz sinusoid. The f(m) power spectrum is shown in Fig. 18(a). The e(m) spectra before and after control are shown in Figs. 18(b) and (c) where an 8th-order FIR filter was used for control. The correlated part of e(m) was well attenuated after control was applied, but the uncorrelated part was amplified somewhat. Again, many frequency components of the correlated part of the e(m) spectrum were attenuated by use of a relatively low order filter.

Figure 19 shows mean-square acceleration level across the span of the beam for this last FM experimental Case 2. The contribution from the second mode was again evident in the uncontrolled response. The best attenuation was near the error sensor with about 25-dB attenuation between x_1 and x_3 and steadily decreasing attenuation between x_3 and x_7, with location x_7 experiencing a slight amplification. The global acceleration-level attenuation was again moderate at 9 dB because of the off-resonance excitation. Attenuation at the frequencies of the carrier and first five sideband pairs was achieved at locations x_1 through x_6 except for x_6 where the third lower sideband was amplified. Measurement location 7 indicated an attenuation for the lower sidebands, but amplification for the carrier and upper sidebands.

8. DISCUSSION

A. Experiment versus simulation

Computer simulations were performed to predict the attenuation that might be achieved in the experiment. Because of the discrepancy between the experimental and theoretical natural frequencies, the excitations used in the simulations were different from those used in the experiments, but were chosen so that proximity of the excitations to the natural frequencies were similar. For example, a 266-Hz carrier with 15-Hz modulation in the experiment for AM Case 1 was replaced with a 308-Hz carrier and 15-Hz modulation in the simulation. In both cases, the car-

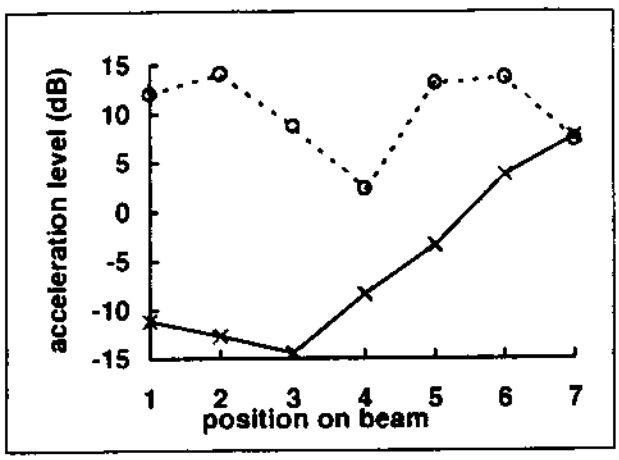

Fig. 19 – Mean-square acceleration level across the span of the beam for FM Case 2. ⊙ no control; × after control.

rier was at the second natural frequency and the sidebands were spaced 15 Hz below and above the carrier frequency.

Results of the computer simulations agreed qualitatively with the experimental results, but predicted between 2- and 10-dB greater acceleration-level attenuations than were measured. In agreement with the experiments, the simulations predicted greater attenuations for the on-resonance cases than for the off-resonance cases. For any individual case, the experimental and simulation plots of attenuation versus measurement location were similar in shape, but the simulations predicted greater attenuation. Limitations of the simulation that may explain some of the discrepancies are described below.

1. Lower damping in the simulations than in the experiments

A modal damping ratio of 0.01 was used for all modes in the simulations while the modal tests in the experiments showed that the damping ratios were somewhat greater. The simulation for AM Case 1 was rerun with the following damping ratios to reflect more accurately the damping in the experiment: $\zeta_1 = 0.06$, $\zeta_2 = 0.03$, $\zeta_n = 0.02$ $(n = 3\text{–}7)$. Figure 20 shows the attenuation of mean-square acceleration level for the experimental and two simulation (low and high damping) results. Although the increased damping improved the agreement between simulation and experiment, other factors also affected the agreement. Moreover, the increased damping provided by the shakers was highly localized while the simulations only incorporated proportional damping.

2. No shaker dynamics included in the simulations

The interaction between the shaker and beam dynamics affected the modal structure of the experimental beam-shakers system by changing the natural frequencies and mode shapes as well as the modal density. These influences were not included in the simulations.

3. Modal truncation in the simulations

The simulation used only the first seven beam modes. For the on-resonance cases, inclusion of just seven modes should have been sufficient as the response was dominated by one mode. For the off-resonance cases where the response was controlled by the sum of a large number of modes, modal truncation effects may have been important.

B. Additional modulation cases

In addition to the cases reported in this paper, two additional AM and two additional FM cases were studied. The carrier frequencies in these cases were the same as above, but the 15-Hz modulation frequency was replaced by modulation frequencies in the 62- to 190-Hz range. The greater modulation frequencies caused wider-band excitations than in the cases reported in this paper.

Again, large attenuation occurred for cases where structural resonances were excited, with moderate attenuation for off-resonance excitation. The off-resonance wideband AM and FM cases both experienced slow convergence in the simulations. The off-resonance wideband AM case in the experiment also had a convergence problem.

The 90-s convergence time limit was increased to 3600 s with the results shown in Fig. 21 along with the results for the 90-s convergence as well as the computer simulation

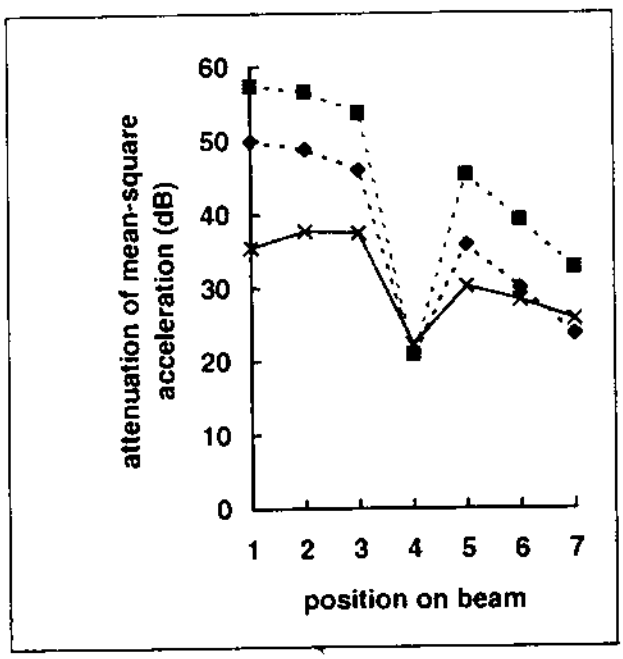

Fig. 20 – For AM Case 1, improved agreement between simulation and experimental determinations of attenuation of mean-square acceleration level. × experiment; ■ simulation (low damping); ◆ simulation (high damping).

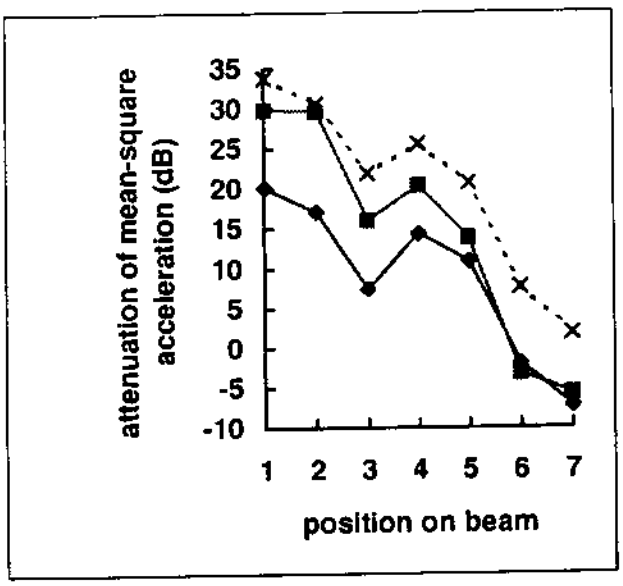

Fig. 21 – For the off-resonance wideband amplitude-modulated case, agreement between simulation and experimental determinations of attenuation of mean-square acceleration level. ◆ experiment (90-s convergence); ■ experiment (3600-s convergence); × simulation.

prediction. Allowing a greater convergence time greatly increased the attenuation in the vicinity of the error sensor and improved the agreement between simulation and experiment. Because the measurement locations farthest from the error sensor were relatively unaffected by the longer convergence time, the global acceleration-level attenuation was only improved by 1 dB from 4 dB to 5 dB.

In all the cases, an 8th-order or lower FIR filter gave the best attenuation in the 90-s time limit except for the off-resonance wideband FM case where a 42nd-order filter gave the best attenuation. The attenuation by the large-order filter may be a result of the suppression of the time-varying terms in the adaptive process that a large filter can provide as shown by Clark and Gibbs.[19] On the other hand, an 8th-order filter also gave good attenuation.

9. CONCLUSIONS

The feasibility of attenuating amplitude- and frequency-modulated vibration disturbances using adaptive feedforward control was demonstrated experimentally. Cases where the disturbance spectrum excited structural resonances experienced greater vibration attenuation than off-resonance cases. When the excitation had frequency components both at and away from resonances, the on-resonance frequency components were attenuated the most while the off-resonance components were attenuated simultaneously as well.

This study also revealed important sound quality issues, though they were beyond the scope of this paper. The beam radiated very efficiently when the excitation was centered at the second beam resonance. The resulting sound was extremely annoying because of the modulation effects. When the active control was applied to the beam, the vibration and hence the radiated noise were reduced with pronounced subjective effects.

Future attempts at predicting vibration control performance using computer simulations should employ realistic damping as well as the inclusion of actuator dynamics to attain better agreement between experimental and simulation results. A rigorous analytical study might be based on a recent theory[21] that predicts modulation sidebands associated with a class of mechanical oscillators.

10. ACKNOWLEDGMENT

The authors acknowledge the primary support from the U.S. Army Research Office (URI Grant DAAL 03-92-G-0120; 1992-1997). The Project Monitor was Thomas L. Doligalski.

11. REFERENCES

[1] R. H. Spencer, M. J. Burke, and G. W. Tye, "Active control of helicopter transmission noise," AHS-RAeS International Technical Specialists Meeting: Rotorcraft Acoustics and Rotor Fluid Dynamics (15–17 October 1991).

[2] G. Wesley Blankenship and Rajendra Singh, "New rating indices for gear noise based upon vibro-acoustic measurements," Noise Control Eng. J. **38**(2), 81–92 (1992 March–April).

[3] Robert L. Clark and Chris R. Fuller, "Experiments on active control of structurally radiated sound using multiple piezoceramic actuators," J. Acoust. Soc. Am. **91**(6), 3313–3320 (June 1992).

[4] C. R. Fuller, C. H. Hansen, and S. D. Snyder, "Active control of sound radiation from a vibrating rectangular panel by sound sources and vibration inputs: An experimental comparison," J. Sound Vib. **145**(2), 195–215 (1991).

[5] C. R. Fuller, C. H. Hansen, and S. D. Snyder, "Experiments on active control of sound radiation from a panel using a piezoceramic actuator," J. Sound Vib. **150**(2), 179–190 (1991).

[6] V. L. Metcalf, C. R. Fuller, R. J. Silcox, and D. E. Brown, "Active control of sound transmission/radiation from elastic plates by vibration inputs, II: Experiments," J. Sound Vib. **153**(3), 387–402 (1992).

[7] Jerome P. Smith, Chris R. Fuller, and Ricardo A. Burdisso, "Control of broadband radiated sound with adaptive structures," Proc. SPIE Conf. Smart Structures Adaptive Materials (February 1993).

[8] J. S. Vipperman, R. A. Burdisso, and C. R. Fuller, "Active control of broadband structural vibration using the LMS adaptive algorithm," J. Sound Vib. **166**(2), 283–299 (1993).

[9] Lisa A. Sievers and Andreas H. von Flotow, "Comparisons and extensions of control methods for narrowband disturbance rejection," IEEE Trans. Signal Process. **40**(10), 2377–2391 (1992).

[10] H. Ming Chen and Paul Lewis, "Adaptive control for a vibration isolation mount," ASME Active Control of Noise and Vib., pp. 121–124 (1992).

[11] Steven J. Elliott, Ian M. Stothers, and Phillip A. Nelson, "A multiple error LMS algorithm and its application to the active control of sound and vibration," IEEE Trans. Acoustics Speech Signal Process. **35**(10), 1423–1434 (1987).

[12] P. A. Nelson and S. J. Elliott, *Active Control of Sound* (Academic, London, 1992).

[13] Bernard Widrow and Samuel D. Stearns, *Adaptive Signal Processing* (Prentice-Hall, Englewood Cliffs, New Jersey, 1985).

[14] Hwei P. Hsu, *Fourier Analysis* (Simon and Schuster, New York, 1970).

[15] Phillip F. Panter, *Modulation, Noise, and Spectral Analysis Applied to Information Transmission* (McGraw-Hill, New York, 1965).

[16] Willliam T. Thomson, *Theory of Vibration with Applications* (Prentice Hall, Englewood Cliffs, New Jersey, 1993).

[17] Andrew D. Dimarogonas and Sam Haddad, *Vibration for Engineers* (Prentice-Hall, Englewood Cliffs, New Jersey, 1992).

[18] John R. Treichler, C. Richard Johnson, Jr., and Michael G. Larimore, *Theory and Design of Adaptive Filters* (Wiley, New York, 1987).

[19] Robert L. Clark and Gary P. Gibbs, "A novel approach to feedforward higher harmonic control," J. Acoust. Soc. Am. **96**(2), 926–936 (August 1994).

[20] Robert L. Clark, Gary P. Gibbs, Chris R. Fuller, "An experimental study implementing model reference active structural acoustic control," J. Acoust. Soc. Am. **93**(6), 3258–3264 (June 1993).

[21] G. W. Blankenship and R. Singh, "Analytical solution for modulation sidebands associated with a class of mechanical oscillators," J. Sound Vib. **179**(1), 13–36 (1995).